Materials Today Bio 31 (2025) 101573

Contents lists available at ScienceDirect

Materials Today Bio

journal homepage: www.journals.elsevier.com/materials-today-bio

Biomimetic mineralized DCPA/ anti-CD47 containing thermo-sensitive injectable hydrogel for bone-metastatic prostate cancer treatment

Shenglong Tan [a,1], Qianqian Wang [b,1], Chunxiang Feng [b,1], Xiaoyong Pu [b], Dong Li [b], Fenglian Jiang [b], Jian Wu [b], Shang Huang [b], Junhong Fan [b], Ruijuan Zhong [c], Chunmiao Mo [a], Jiayu Luo [a], Peiliang Zhong [a], Jiumin Liu [b,**], Dandan Ma [a,*]

[a] Department of Endodontics, Stomatological Hospital, School of Stomatology, Southern Medical University, Guangzhou, 510280, China
[b] Department of Urology, Guangdong Provincial People's Hospital (Guangdong Academy of Medical Sciences), Southern Medical University, Guangzhou, 510080, China
[c] Department of Operating Room, Guangdong Provincial People's Hospital (Guangdong Academy of Medical Sciences), Southern Medical University, Guangzhou, 510080, China

ARTICLE INFO

Keywords:
Biomimetic mineralization
DCPA
M1 macrophage polarization
Anti-tumor immunity
Prostate cancer bone metastasis

ABSTRACT

Strategies that leverage the phagocytic capabilities of M1 macrophages against tumor cells are currently being investigated for cancer treatment. However, the clinical application of these strategies is significantly hampered by the severe side effects associated with conventional M1 macrophage activators. In this study, biomimetic mineralized dicalcium phosphate anhydrous (MDCPA) was synthesized using Zein as an organic template, aiming to promote M1 macrophage polarization effectively while minimizing side effects. *In vitro* experiments demonstrated that MDCPA can be engulfed by macrophages and induce M1 macrophage polarization. By combining the stimulation of MDCPA with a commonly used immune checkpoint inhibitor, anti-CD47 (aCD47), the macrophages exhibited the highest phagocytic activity toward prostate cancer cells. Further *in vivo* experiments illustrated significant tumor suppression and reduced bone resorption in a prostate cancer bone metastasis model utilizing MDCPA/aCD47-containing thermos-sensitive injectable hydrogels (MDCPA/aCD47 TSI gel). Mechanistic studies indicated that the MDCPA/aCD47 TSI gel promotes tumor cell apoptosis not only through the phagocytosis of tumor cells mediated by M1 macrophages, but also by activating anti-tumor CD8-positive T cells. Consequently, this composite gel platform presents an effective theragnostic strategy for treating prostate cancer bone metastasis without the associated side effects, facilitated by biomimetic minerals that mediate anti-tumor immunity.

1. Introduction

Bone metastasis is a common complication in the advanced stages of prostate cancer (PCa) [1]. Skeletal complications, such as pain and ineffective hematopoiesis, significantly affect the quality of life and survival of patients [2]. Androgen deprivation therapy (ADT), in combination with bone-targeted agents (such as bisphosphonates), taxane-based chemotherapy (docetaxel) or synthetic corticosteroid analog (prednisone), is commonly employed for these patients. However, tumor often relapse within the first year due to the resistance of tumor cells to chemotherapy [3]. In addition to genetic alterations in tumor cell that result in active resistance, macrophages in the tumor microenvironment have been reported as a key regulator of the resistance. For instance, macrophages can activate STAT3 in tumor cells by secreting inflammatory factors, which enhances the proliferation and survival of tumor cells [4]. Activated M2 macrophages following chemotherapy can promote tumor revascularization and relapse [5]. Therefore, therapeutic strategies that target or incorporate macrophages have the potential to improve treatment efficacy for bone-metastatic PCa.

Among these strategies related to macrophages targeted cancer immunotherapy [6], immune checkpoint inhibitor therapy, such as anti-CD47(aCD47), and the activation of M1 macrophages have shown notable success. The former therapeutic strategy utilizes aCD47 to

* Corresponding author.
** Corresponding author.
E-mail addresses: jiumin8388@163.com (J. Liu), mdd@smu.edu.cn (D. Ma).
[1] These authors contributed equally to this work.

https://doi.org/10.1016/j.mtbio.2025.101573
Received 19 October 2024; Received in revised form 12 January 2025; Accepted 9 February 2025
Available online 11 February 2025

disrupt the interaction between the overexpressed CD47 on tumor cell and the SIRPα receptor on macrophages, which triggers a "don't eat me" signal, thereby enabling macrophages to recognize and phagocytose tumor cells [7]. Additionally, effective delivery of cytokines significantly enhances prostate cancer (PCa) therapy. Recently, thermosensitive injectable gels (TSI gels), including thermosensitive hydrogels based on PLGA-PEG-PLGA triblock copolymers [8], polyamino acid injectable thermosensitive hydrogel [9], hyaluronic acid-Pluronic F127 injectable thermosensitive hydrogels [10], have garnered increased attention. Beyond their role as drug carriers and their injectability, the most significant advantage of TSI gels is their ability to solidify in situ at body temperature, which helps to preserve the drug during intratumoral injection and improves treatment outcomes [11]. The later therapeutic strategy leverages the phagocytic capabilities of activated M1 macrophages to combat tumor cells, thereby suppressing tumor progression [12]. To date, various methods have been employed to activate M1 macrophages, including small-molecule inhibitors, such as PI3K-γ [13] and tumor vaccines containing granulocyte–macrophage colony-stimulating factor (GM-CSF [14]). However, these inhibitors or factors often bring inevitable side effects, including toxicity, resistance or mild to moderate medullary bone pain [15,16].

To balance safety and effectiveness, calcium phosphate biomaterials (CaPs) have been utilized as an alternative due to their biocompatibility and immunomodulatory effects. On one hand, CaPs, such as calcium-deficient hydroxyapatite (CDHA), have been reported to stimulate macrophages M1 polarization [17,18] which may be attribute to the rapid release of Ca^{2+} [19] that induce Ca^{2+} influx in macrophages [20]. On the other hand, CaP particles can enhance the inflammatory response and phagocytic activity of macrophages [21,22]. As one of hydroxyapatite precursors, dicalcium phosphate anhydrous (DCPA, $CaHPO_4$),

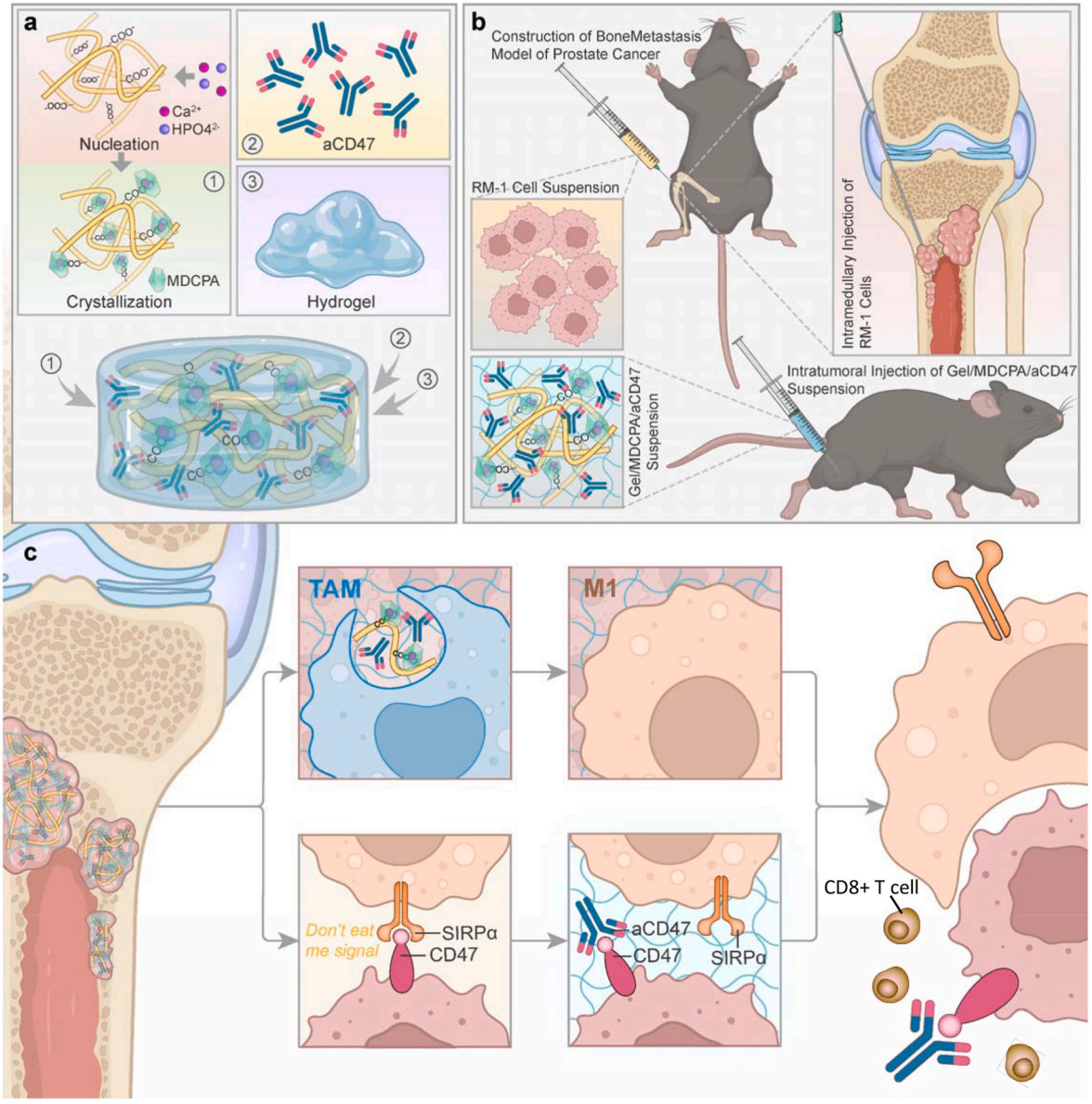

Scheme 1. The principles of treating bone-metastatic prostate cancer using MDCPA/aCD47@TSI gel. (a) The fabrication of the MDCPA/aCD47 containing hydrogel. Involved the preparation of MDCPA through Zein-based biomineralization. Subsequently, MDCPA, aCD47 and hyaluronic acid/Pluronic F-127 TSI hydrogel were mixed to obtain a composite hydrogel. (b) To construct a bone-metastatic prostate cancer model, an RM-1 cell suspension was injected, followed by the application of the composite hydrogel via intratumoral injection for cancer treatment. (c) The schematic diagram illustrates three mechanisms that promote tumor cell death: 1. MDCPA enhances the phagocytic activity of macrophages towards cancer cells by inducing M1 macrophage polarization; 2. aCD47 binds to the CD47 receptor on cancer cells, blocking the 'Don't eat me' signal, which promotes the phagocytosis of cancer cell; 3. The composite hydrogel enhances the activity of $CD8^+$ T cell, which assist in the elimination of tumor cells.

which has a low Ca/P atomic ratio, exhibits higher solubility than the thermodynamically stable CDHA or HA [23–25]. This suggests that DCPA may stimulate macrophages M1 polarization more effectively by releasing a significant amount of calcium ions. However, current research has primarily focused on the response of DCPA to osteoclasts derived from macrophages, particularly in terms of degradation and absorption [26,27], indicating that the bioactivity of DCPA may be insufficient to directly activate macrophages response. Biomimetic mineralization, an emerging strategy in biomaterial fabrication, has shown promise in further enhancing the macrophage response of CaPs. For instance, biomimetic hydroxyapatite has demonstrated superior degradation potential through macrophage-mediated phagocytosis [28] compared to synthetic hydroxyapatite. Therefore, biomineralization strategy may serve as an effective approach to improve the bioactivity of DCPA by enhancing macrophage-mediated phagocytosis. However, the preparation of DCPA has been largely restricted to chemical synthesis methods [29], and there has been limited research on the fabrication of DCPA via biomineralization.

Moreover, considering the efficiency of a single strategy in promoting macrophage-mediated phagocytosis is limited, the combination of multiple strategies to promote macrophage-mediated phagocytosis may achieve a synergistic effect [30]. While to date, few studies have reported that the combination of biomimetic mineralized calcium and phosphorus materials stimulated M1 macrophage polarization and aCD47 synergistically enhanced macrophage-mediated phagocytosis against tumor cells. In this study, biomimetic mineralized DCPA (MDCPA) was prepared through biomineralization using Zein, a non-collagen protein derived from plant rich in acidic amino acids, as the organic template and acidic artificial saliva as the mineralized medium. Subsequently, MDCPA combined with aCD47 were co-loaded into thermosensitive injectable hydrogels (TSI gel) to construct a composite hydrogel (MDCPA/aCD47@TSI gel) for the treatment of bone-metastatic prostate cancer (Scheme 1). Following intratumoral injection, the MDCPA/aCD47@TSI gel cured in situ and exhibited multiple anti-tumor effects: 1. MDCPA was phagocytosed by macrophages, stimulating the polarization of macrophages towards the M1 phenotype and enhancing their phagocytic activity; 2. aCD47 was released to bind to CD47 on the tumor surface, preventing tumor cells from evading macrophage phagocytosis; 3. The MDCPA/aCD47@TSI gel activated $CD8^+$ T cells, which assist in the elimination of tumor cells. The results demonstrated that the MDCPA/aCD47@TSI gel effectively suppressed prostate cancer progression and bone resorption, suggesting significant potential for the treatment of bone-metastatic prostate cancer.

2. Results

2.1. Preparation and characterization of MDCPA

As illustrated in Fig. 1a, MDCPA was prepared using Zein as an organic template and acidic artificial saliva (pH = 6.68) as the mineralization medium through a biomineralization process. The results of the ion concentrations changes during biomineralization indicated that the concentrations of calcium and phosphorus ions remained relatively stable after 3 days (Fig. S1), suggesting that the biomineralization process was nearly complete within this timeframe. Subsequently, the factors influencing MDCPA yield were analyzed, as shown in Fig. S2. It revealed that the yield of MDCPA was maximized at a mineralization pH of 6.68, a Zein mass of 0.1g, and a mineralization duration of 3 days. The phase composition and surface morphology of MDCPA were then characterized. The XRD results presented in Fig. 1b indicated that the phase composition of MDCPA was primarily $CaHPO_4$, as confirmed by comparison with the JCPDS data for DCPA (090080). The analysis of the thermal degradation product of MDCPA and DCPA provides valuable insight. The thermogravimetric (TG) results presented in Fig. 1c indicate that DCPA exhibited a weight loss of 8.77 % between 425–455 °C, attributed to the thermal decomposition of $CaHPO_4$, leading to the formation of calcium pyrophosphate ($Ca_2P_2O_7$) [31]. Similarly, MDCPA also demonstrated weight loss in the range of 425~430 °C, with the thermal degradation product identified as $Ca_2P_2O_7$, corroborated by subsequent XRD results. This consistent thermal degradation product indicates a shared inorganic phase between MDCPA and DCPA. It is noteworthy that, despite both DCPA and MDCPA yielding $Ca_2P_2O_7$ as the phase composition of their thermal decomposition products, the JCPDS diffraction data cards differ: JCPDS#23–0871 corresponds to sintered MDCPA, while JCPDS#17–0499 is associated with sintered DCPA. This discrepancy may be attributed to the residual Zein present in MDCPA, which could influence the crystalline structure of $Ca_2P_2O_7$. Furthermore, the surface morphology and elemental distribution of MDCPA are depicted in Fig. 1d, revealing that MDCPA forms plate-like crystals, akin to those of DCPA [32]. Elemental mapping further demonstrated that, in addition to calcium and phosphorus, the surface of MDCPA contains nitrogen element, indicative of organic molecules associated with Zein. This observation suggests that MDCPA function as an inorganic-organic complex, comprising both $CaHPO_4$ and Zein.

2.2. Biomineralization process of MDCPA

To investigate the biomimetic mineralization process of MDCPA, the minerals deposited on Zein at different mineralization times were characterized. SEM results (Fig. 1e and f) indicated that minerals with approximately 200 nm in diameter formed on the surface of Zein after 60 min of mineralization, suggesting the onset of CaP mineral crystallization at this time. Further TEM and elemental analysis presented in Fig. 1g demonstrated that CaP mineral particles were also present within the internal of Zein. Additinally, element mapping shown in Fig. 1h and i revealed that calcium ions (depicted in green) exhibited a more widespread distribution in Zein compared to phosphate ions (depicted in blue), indicating that a preferential deposition of calcium ions followed by the adsorption of phosphate ions, which may trigger the nucleation and growth of mineral crystals. Given that Zein is rich in acidic amino acids, it is plausible that calcium ions may be caught by acidic amino acids via electrostatic interaction [33]. After 72 h of mineralization, mineral particles (shown in white) were distinctly visible on the Zein surface, as shown in Fig. 1j. Further confocal laser scanning microscopy (CLSM) images displayed in Fig. 1k revealed that plate-like mineral particles were scattered within Zein. It has been reported that acidic amino acid can adsorb to growing crystals, significantly altering the crystal morphology from needle-like to plate-like by inhibiting both nucleation and growth [34]. The biomineralization mechanism involving Zein may resemble that of biomineralization mediated by acidic amino acids [35,36]. Consequently, it can be speculated that the biomimetic mineralization process of MDCPA initiates with the sequential binding of Ca^{2+} and PO_4^{3-} to the acidic amino acids of Zein, followed by the gradual accumulation of lamellar MDCPA particles (Fig. 1l).

2.3. Physicochemical properties and bioactivity of MDCPA

As a glutamate-rich non-collagen protein [37], the component of Zein resembles the natural bone matrix [38]. This similarity suggests that the composition of MDCPA is akin to that of the native bone matrix, which may confer excellent biological activity, including biomineralizing activity. Previous studies have also reported the assessment of the biological activity of DCPA by analyzing the formation of HA following soaking DCPA into simulated body fluid (SBF) [39], the commonly used mineralization solution [40]. In our study, the biomineralizing activity of MDCPA was assessed using SBF.

Firstly, the release behaviour of Ca^{2+} and PO_4^{3-} ions was investigated, and the results were presented in Fig. 2a. Following the immersion of MDCPA and DCPA in SBF, the concentrations of calcium and phosphorus ions increased rapidly within one day. Furthermore, the

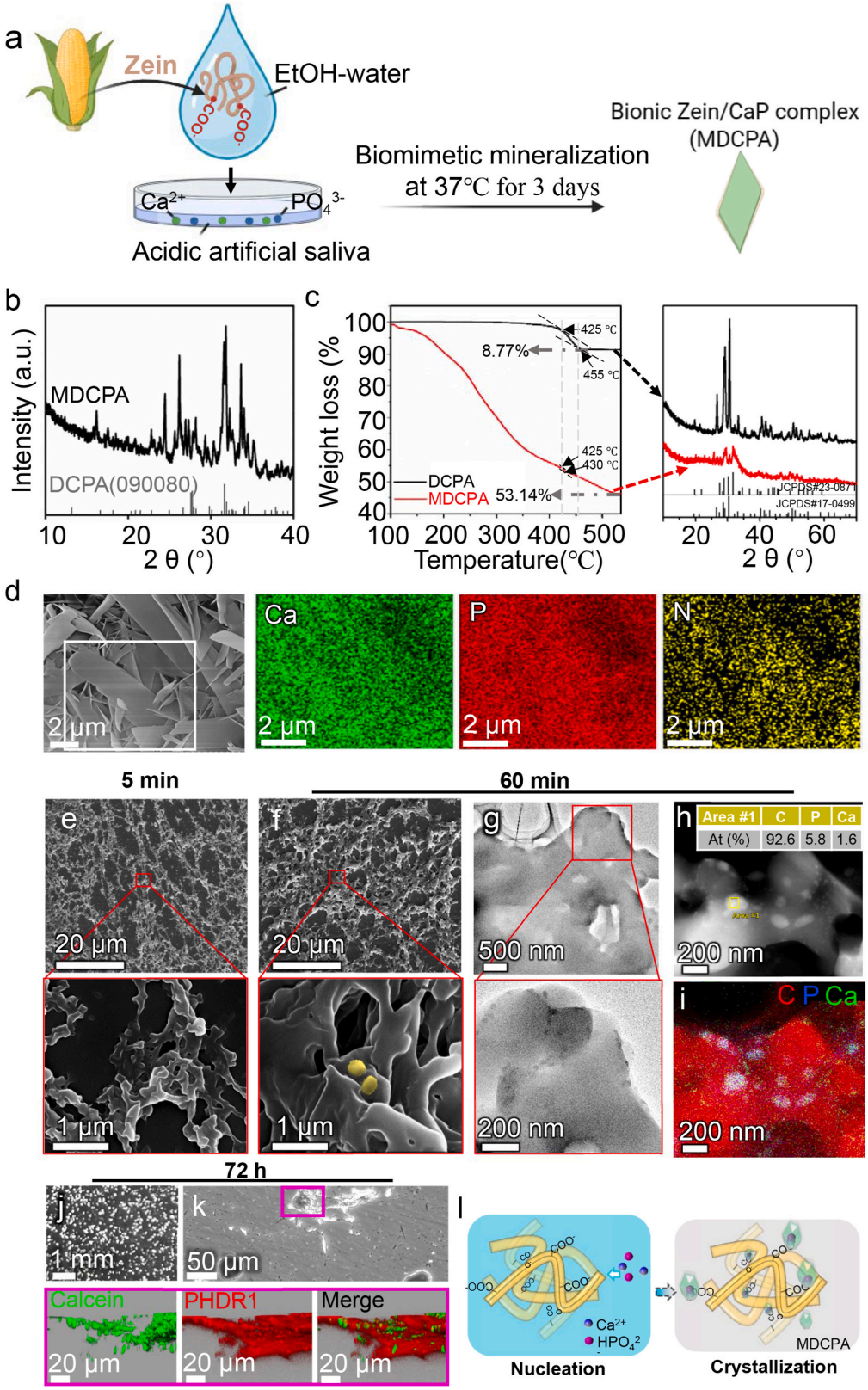

Fig. 1. Illustrates the preparation and characteristics of MDCPA and its biomineralization process. (a) A scheme of the fabrication process of MDCPA. (b) XRD result of MDCPA. (c) Thermogravimetric analysis of MDCPA and DCPA and XRD patterns of MDCPA and DCPA after sintering at 500 °C for 2 h. (d) SEM with element mapping analysis of MDCPA. (e) Surface morphology of Zein after mineralization for 5 min (f, g, h, i) SEM and TEM images of mineralized particles formed in Zein after mineralization for 60 min. (j, k) Digital and CLSM images of MDCPA after mineralization for 3 days. MDCPA was stained with calcein and rhodamine phalloidin (PHDR). (l) Schematic diagram of MDCPA formation via biomineralization process.

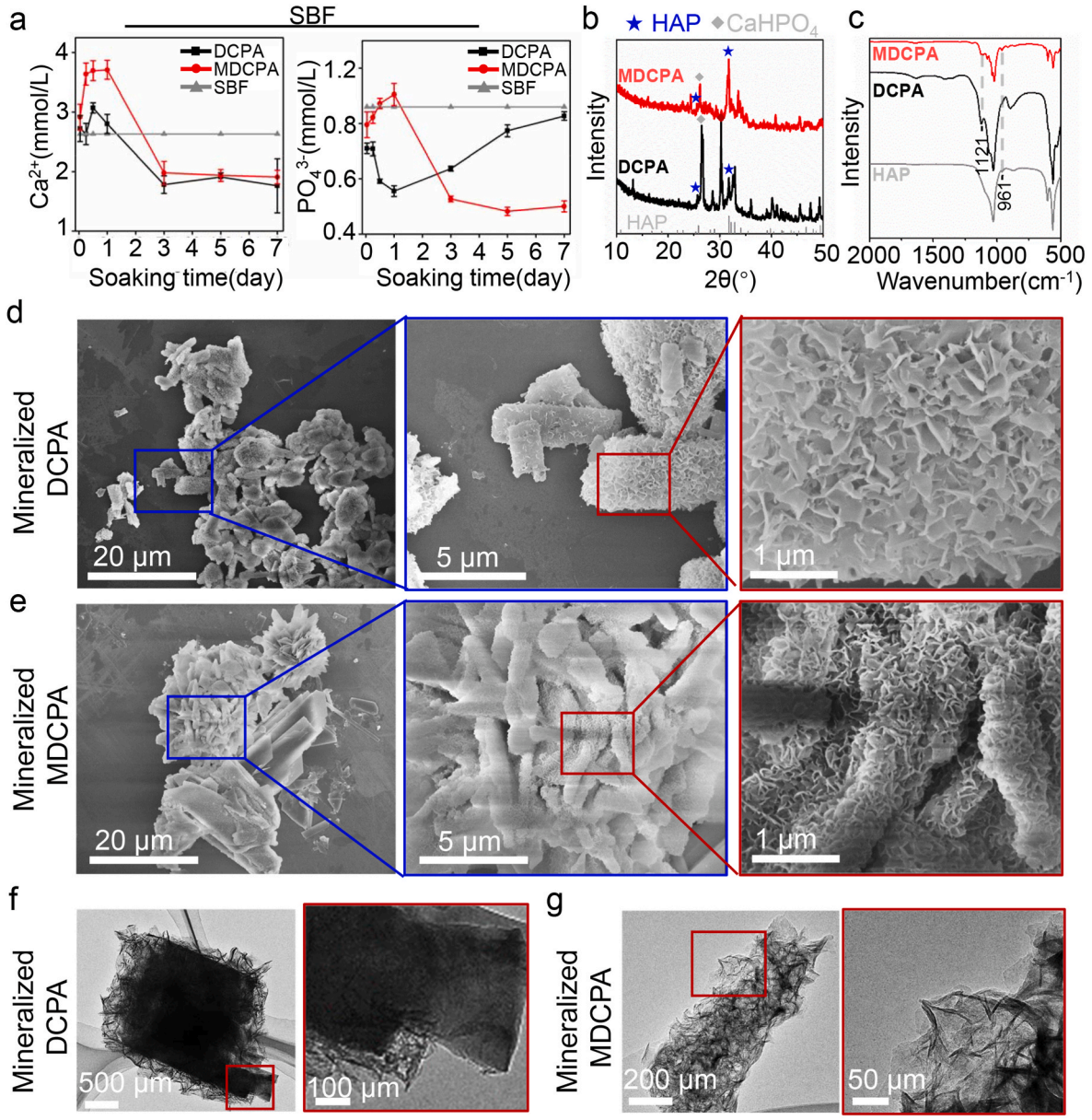

Fig. 2. Physicochemical properties and bioactivity of MDCPA and DCPA. (a) $Ca^{2+}$and PO_4^{3-} ions concentration following the soaking of MDCPA and DCPA in SBFsolution for virous times. (b) XRD, (c) FTIR, (d, e) SEM and (f, g) results of MDCPAand DCPA after mineralization in SBF at 37 °C for 7 days.

concentration of calcium and phosphorus ions were higher in MDCPA compared to DCPA, indicating that Ca^{2+} and PO_4^{3-} ions were released from MDCPA at a faster rate than from DCPA. This observation was corroborated by the results of Ca^{2+} and PO_4^{3-} ions release in PBS solution, a non-mineralized medium (Fig. S3), which also demonstrated that the release of Ca^{2+} and PO_4^{3-} ions from MDCPA was greater than that from DCPA. Subsequently, as time progressed, the concentrationd of calcium and phosphorus ions gradually decreased. This decline can be attributed to the deposition of calcium and phosphorus ions in minerals, signifiying the onset of biomineralization. It was noteworthy that the concentration of phosphorus ions in the DCPA-containg solution began to increase slowly from the third day, indicating a deceleration in the rate of biomineralization. These results also suggested that, compared to DCPA, MDCPA may exhibit a higher biomineralizing activity, as evidenced by ongoing mineralization in MDCPA relative to DCPA. This finding was further corroborated by XRD results presented in Fig. 2b. Although the hydroxyapatite peak was observed in both mineralized products after 7 days of mineralization, the monetite peak decreased significantly in the MDCPA group compared to the DCPA group, indicating that MDCPA underwent a complete transformation to hydroxyapatite. FTIR results in Fig. 2c also revealed that the characteristic peak of hydroxyapatite at 961 cm^{-1} [41] was more prominently observed in the MDCPA group than in the DCPA group. Furthermore, SEM results (Fig. 2d and e) demonstrated that the surfaces of the mineralized products from both MDCPA and DCPA were covered with a mineralized layer. Based on the above XRD and FTIR results, it can be inferred that these minerals were indeed hydroxyapatite. TEM images (Fig. 2f and g) further indicated that the hydroxyapatite crystals were needle-shaped. Additionaly, the flake stucture remained significantly intact after mineralization of DCPA (Fig. 2f); however, it was almost entirely absent following the mineralization of MDCPA (Fig. 2g), suggesting that the transition to hydroxyapatite was inadequate in DCPA, while sufficient in MDCPA. Collectively, these results demonstrate that MDCPA exhibits greater biological activity than DCPA.

2.4. MDCPA promoted M1 macrophages polarization

To investigate the interaction between MDCPA and macrophages, MDCPA was initially labeled with calcein (Fig. S4). The results demonstrated that MDCPA particle can colocalize with calcein (green fluorescence), indicating that MDCPA can be traced by detecting this green fluorescence. Following the co-incubation of calcein labeled mineral and macrophages, mineral particles were visualized under fluorescence microscope, with results presented in Fig. 3a. It displayed that green fluorescence appears inside the macrophages only following the co-incubation with calcein labeled MDCPA, indicating that MDCPA particles were easily engulfed by macrophages comparing with DCPA. This finding was further confirmed by the confocal laser scanning microscopy (CLSM) results, with results presented in Fig. 3b and c. It was observed that following the contacting of calcein-labeled DCPA and macrophages, there was no significant change in the position of the DCPA over time (Fig. 3b), this result was consistent with the fluorescence microscope results in Fig. 3a that the DCPA granules could not be engulfed by macrophages. In contract, the green fluorescence was prominent when MDCPA first contacted the macrophage surface at 0 min under brightfield illumination. Then, MDCPA was enveloped by the cell membrane and entered the cell at 5 min, meantime, the green fluorescence became undetectable. Subsequently, at 15 min, MDCPA gradually moved away from the cell membrane and even fragmented into smaller pieces by 35 min (Fig. 3c), indicating further internalization and degradation. The occurrence of this process explained why more calcein labeled MDCPA appears within macrophages as the results in Fig. 3a. Previous studies have reported that membrane tension increases during the process of phagocytosis [42]. Therefore, to confirm whether the phagocytosis of MDCPA particles dependent on cell membrane tension, cytochalasin D, a potent inhibitor of actin polymerization, was employed. As shown in fluorescence microscopy results (Fig. S5), a great number of calcein-labeled MDCPA particles were observed outside of the macrophages following the addition of cytochalasin D, suggesting that cytochalasin D inhibited the phagocytosis of MDCPA particles.

To evaluate the inflammatory response of macrophages after the phagocytosis of MDCPA, the expression of pro-inflammatory and anti-inflammatory related gene (IL-10 [43], IL-6 [44], CD206 and CCR7 [45]) in macrophages were evaluated and shown in Fig. 3d. It displayed that following the stimulation of MDCPA, the expression of pro-inflammatory related gene: IL-6 were upregulated, while the anti-inflammatory related gene CD206 was significantly upregulated in macrophages compared to DCPA, indicating that MDCPA may stimulate macrophages to differentiate in the direction of pro-inflammatory M1 macrophages in contrast to DCPA. This finding was confirmed by measuring the concentration of IL-6 and IL-10 in the macrophage medium after coincubation with MDCPA for 24 h. As the ELISA results in Fig. 3e, the IL-10 levels in the MDCPA group were significantly lower than those in the IL-4 group, while the concentration of IL-6 in the MDCPA group was significantly higher than that in the LPS group. Given that IL-4 and LPS are commonly used factors to promote M2 and M1 macrophages polarization, respectively [46], we can conclude that the phagocytosis of MDCPA may induce M1 macrophage polarization. Further RNA-seq results demonstrated the possible mechanism that MDCPA stimulated M1 polarization of macrophages. Go analysis results in Fig. 6a showed that immune system related biological process was enhanced in macrophages. KEGG analysis results in Fig. 6b displayed that TNF signaling pathway was upregulated in macrophages. For TNF had been reported to promote M1 polarization [47], MDCPA may induce M1 macrophage polarization through TNF signaling pathway.

2.5. MDCPA combined with aCD47 enhanced the phagocytosis of tumor cells

M1 macrophages have been reported to directly engulf tumor cells through their phagocytic capabilities [48]. This suggests that as a mineral that can stimulate M1 macrophage polarization, MDCPA may have the potential to enhance macrophage phagocytosis of tumor cells. However, one significant factor that weakens the phagocytic effect of M1 macrophages is the CD47 receptor on cancer cells, which binds to SIRPα on the surface of macrophages, resulting in the release of the 'do not eat me' signal (Fig. 4a). Anti-CD47 (aCD47) has been shown to block the CD47 receptor, thereby reducing the CD47-SIRPα binding and enhancing the phagocytosis of tumor cells by macrophages [49]. Consequently, we hypothesize that the combination of MDCPA and aCD47 can effectively promote the phagocytosis of tumor cells. To verify this hypothesis, bone marrow-derived macrophage cells (BMDMs) were first extracted and identified using flow cytometry, as Fig. 4b, c the results indicated that the extracted cells were $CD11b^{+}F4/80^{+}CD80^{+}$, confirming their identity as macrophages. Subsequently, mouse prostate cancer cell (RM-1 cells) were co-incubated with BMDMs in presence of MDCPA and aCD47. Observations from luminescence microscope observation (Fig. 3d) revealed a higher degree of co-localization between RM-1 cancer cells and BMDMs (indicated by white circular dashed line) in the MDCPA/aCD47 group compared to the MDCPA or aCD47 group. Further flow cytometric analysis, as shown in Fig. 4e, also indicated that the phagocytosis of RM-1 cancer cells by BMDMs occurred in the following order: MDCPA/aCD47 group > MDCPA group > aCD47 group > Control group. These results suggest that MDCPA significantly enhances the phagocytic activity of macrophages, demonstrating greater efficacy than the commonly used small molecule inhibitor-aCD47 [50]. This enhancement can be attributed to the phagocytic effect of M1 macrophages induced by MDCPA on tumor cells. Importantly, macrophages in the MDCPA/aCD47 group exhibited the highest tumor cell phagocytic activity, indicating that MDCPA acts as an enhancer that synergizes with aCD47 to effectively promote macrophage phagocytosis to tumor cells.

2.6. MDCPA/aCD47@TSI gel suppressed the progression of bone-metastatic prostate cancer

Pluronic F127 has been wide used as a thermos-sensitive injectable (TSI) hydrogel for intratumoral delivery [51]. In this study, a hyaluronic acid/Pluronic F-127 TSI hydrogel was prepared through the physical mixing of hyaluronic acid, Pluronic F-127 and DMEM medium with modifications based on existing literature [52]. As shown in Fig. 5a, the transmittance of TSI gel rapidly decreased when the temperature dropped to 28 °C, indicating that the TSI gel can undergo a sol-gel phase transition at this temperature. Further digital images in Fig. 5b demonstrated that the TSI gel lost its fluidity at 37 °C, suggesting that body temperature would solidify the TSI gel following intratumoral injection. Subsequently, the cumulative release of aCD47 from the TSI gel, with or without MDCPA, is illustrated in Fig. 5c. The release behaviors of aCD47 from both gels were similar, characterized by an explosive release of aCD47 within the first 12 h, followed by a slower release over 6 days. The key difference observed was that a greater amount of aCD47 was released from the MDCPA/aCD47@ TSI gel compared to the aCD47@ TSI gel, indicating that the addition of MDCPA enhanced the release of aCD47 from the TSI gel.

Fig. 5d presents a schematic representation of bone metastases in prostate cancer treatment utilizing MDCPA/aCD47@TSI gel. Initially, a mouse model of bone metastases in prostate cancer was established by injecting RM-1 cells into the tibia of the mouse, which was subsequently confirmed through bioluminescence imaging. Following this, MDCPA/aCD47@TSI gel was administered intratumorally to the tumor. The therapeutic effects were monitored via bioluminescence imaging, with results illustrated in Fig. 5e, f. It was observed that the total fluorescence intensity in the MDCPA/aCD47@TSI gel(G5) group did not significantly differ from that of the other groups at day 0; however, a marked decrease was noted when compared to the other groups at day 6, indicating significant anti-cancer effects. Additionally, Fig. 5g depicts the weight changes of mice with bone-metastatic prostate cancer following

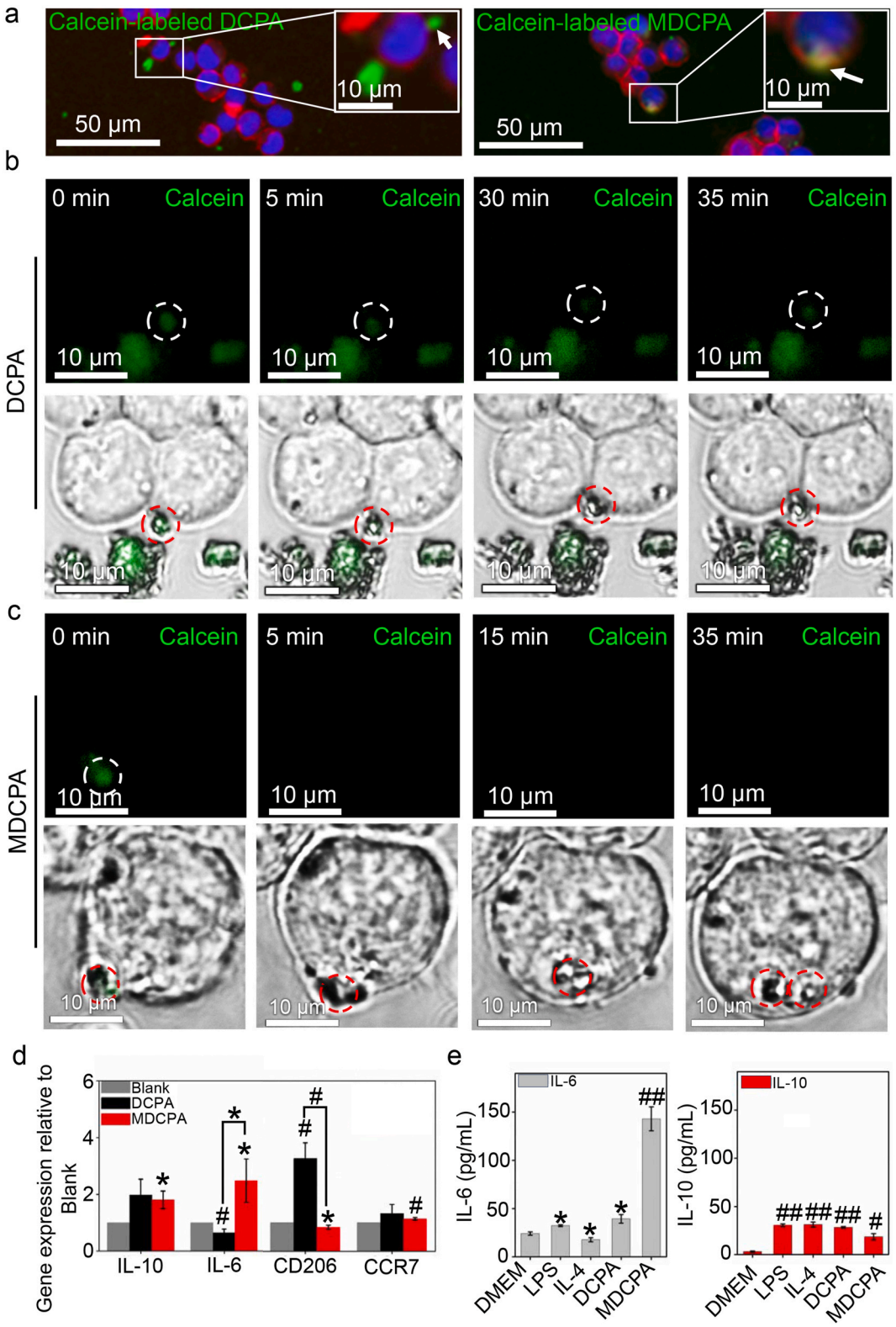

Fig. 3. MDCPA enhanced the phagocytic activity of macrophages. (a) Fluorescence microscopy images of calcein-labeled minerals and RAW264.7 cells. (b, c) Confocal laser scanning microscopy images of calcein-labeled minerals and RAW 264,7 cells at various time points. (d) Relative gene expression of IL-10, IL-6, CD206 and CCR7 in macrophages after a 24-h co-incubation with mineral suspension of 125 μg/mL (e) ELISA analysis of the concentrations of IL-6 and IL-10 in the culture medium of RAW264.7 cells following stimulation with LPS (100 ng/mL), IL-4 (20 ng/mL) and MDCPA suspension (125 μg/mL) for 24 h.

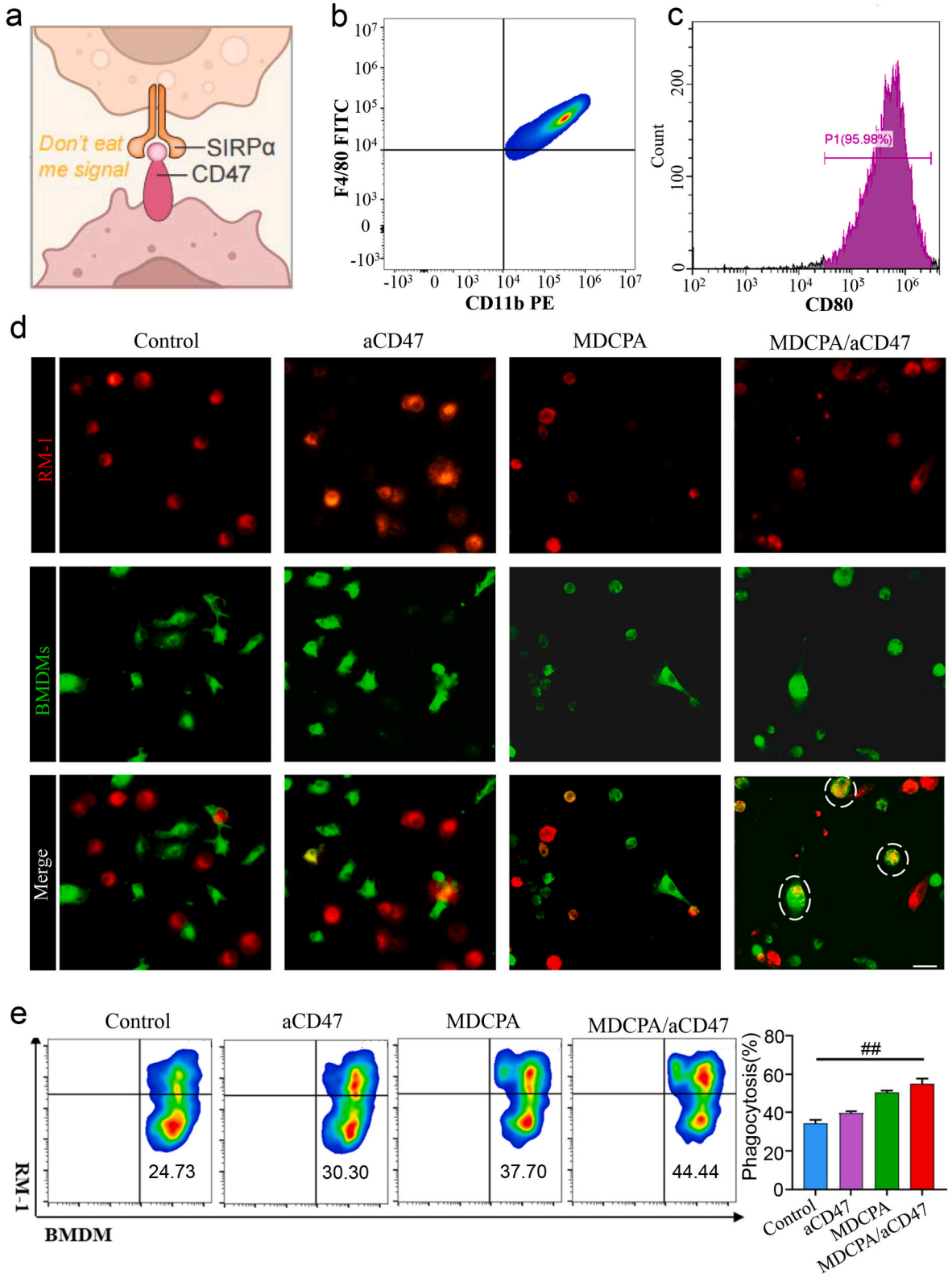

Fig. 4. CD47 blockade enhances phagocytosis *in vitro*. (a) A schematic diagram of CD47-SIRPα immune checkpoint. (b) Flow cytometry analysis of bone-marrow-derived macrophage cells (BMDMs) markers: CD11b and F4/80. (c) Flow cytometry analysis of M1 Macrophage polarization markers: CD80. (d) Representative images of phagocytosis assays, where RM-1 cancer cells were labeled with CellTracker DeepRed (red) and BMDMs were labeled with CellTracker Green (green). Scale bar, 100 μm. Experiments conducted in triplicate. (e) Representative flow cytometric analysis images (left) and relative quantification (right) of the phagocytosis of cancer cells by BMDMs. Data are presented as mean ± SEM (n = 3). Phagocytosis was quantified as the percentage of double-positive BMDMs among CellTracker Green-positive BMDMs or CellTracker DeepRed-labeled cancer cells.

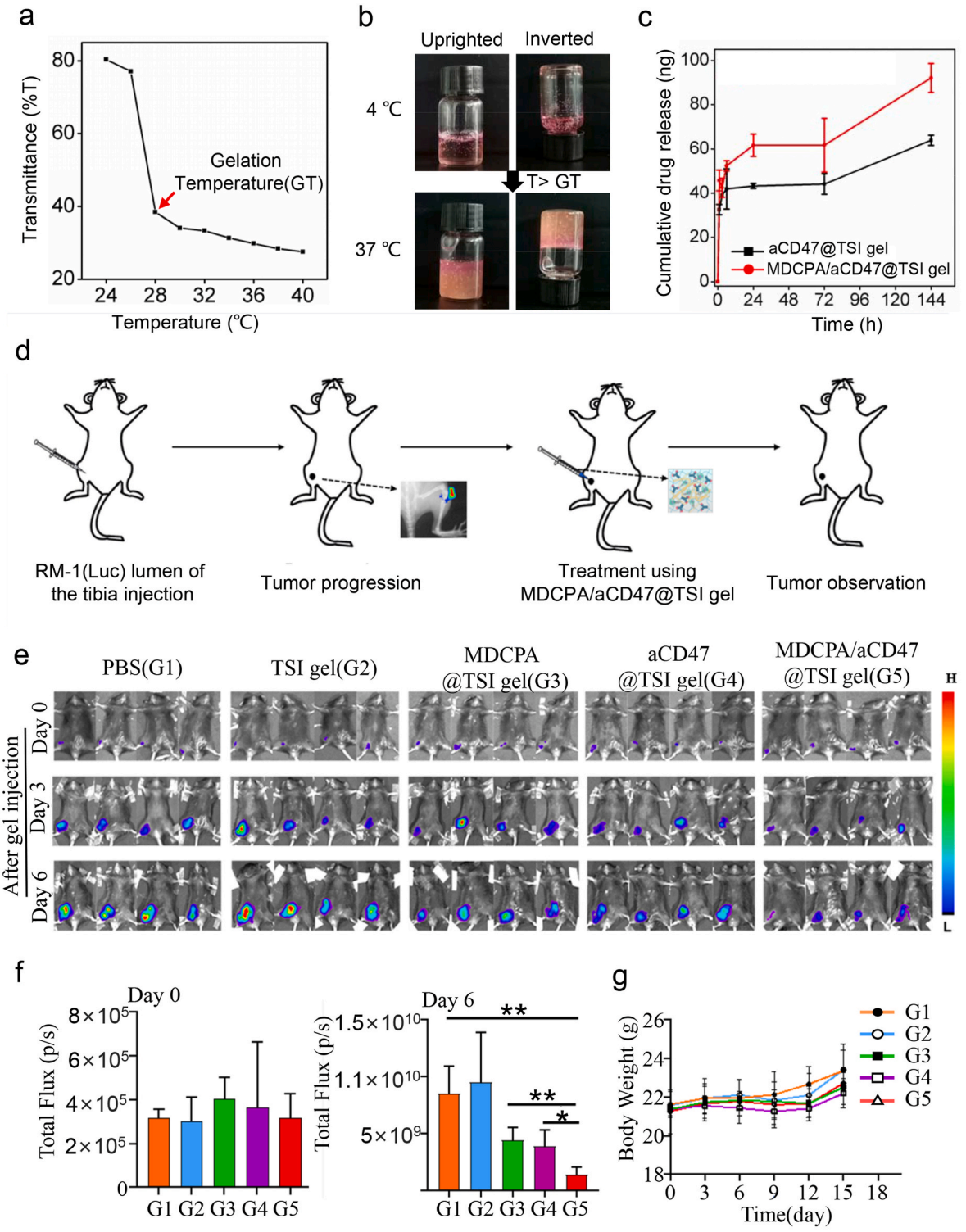

Fig. 5. MDCPA/aCD47@TSI gel and its impact on the treatment of bone-metastatic prostate cancer. (a) Light-transmittance measurement at 500 nm for the MDCPA/aCD47@TSI gel as a function of temperature. (b) Digital images of the MDCPA/aCD47@TSI gel at temperature of 4 °C and 37 °C. (c) Cumulative drug release of aCD47 from either the aCD47@TSI gel or the MDCPA/aCD47@TSI gel over varying soaking times. (d) Schematic illustrating MDCPA/aCD47@TSI gel therapy in a mouse model of bone-metastatic prostate cancer. (e) In vivo bioluminescence imaging of RM-1 tumors in response to local MDCPA/aCD47@TSI gel treatment, with images taken on day 7 prior to treatment. (f) Total fluorescence intensity from *in vivo* imaging of mice on the day of drug injection and on the sixth day following treatment. (g) Chart of weight changes in mice since the establishment of the tumor model.

treatment with MDCPA/aCD47@TSI gel(G5). The results indicated no significant difference in weight between the G5 group and other groups, suggesting that the use of MDCPA/aCD47@TSI gel did not produce any notable toxic effects *in vivo*. This finding was further corroborated by HE staining of heart, lung, spleen, liver, and kidney sections from these groups (Fig. S8). Further blood analysis results showed that the level of alanine aminotransferase (ALT) and aspartate aminotransferase (AST) in four treated groups(G2~G5) were comparable to those in the control

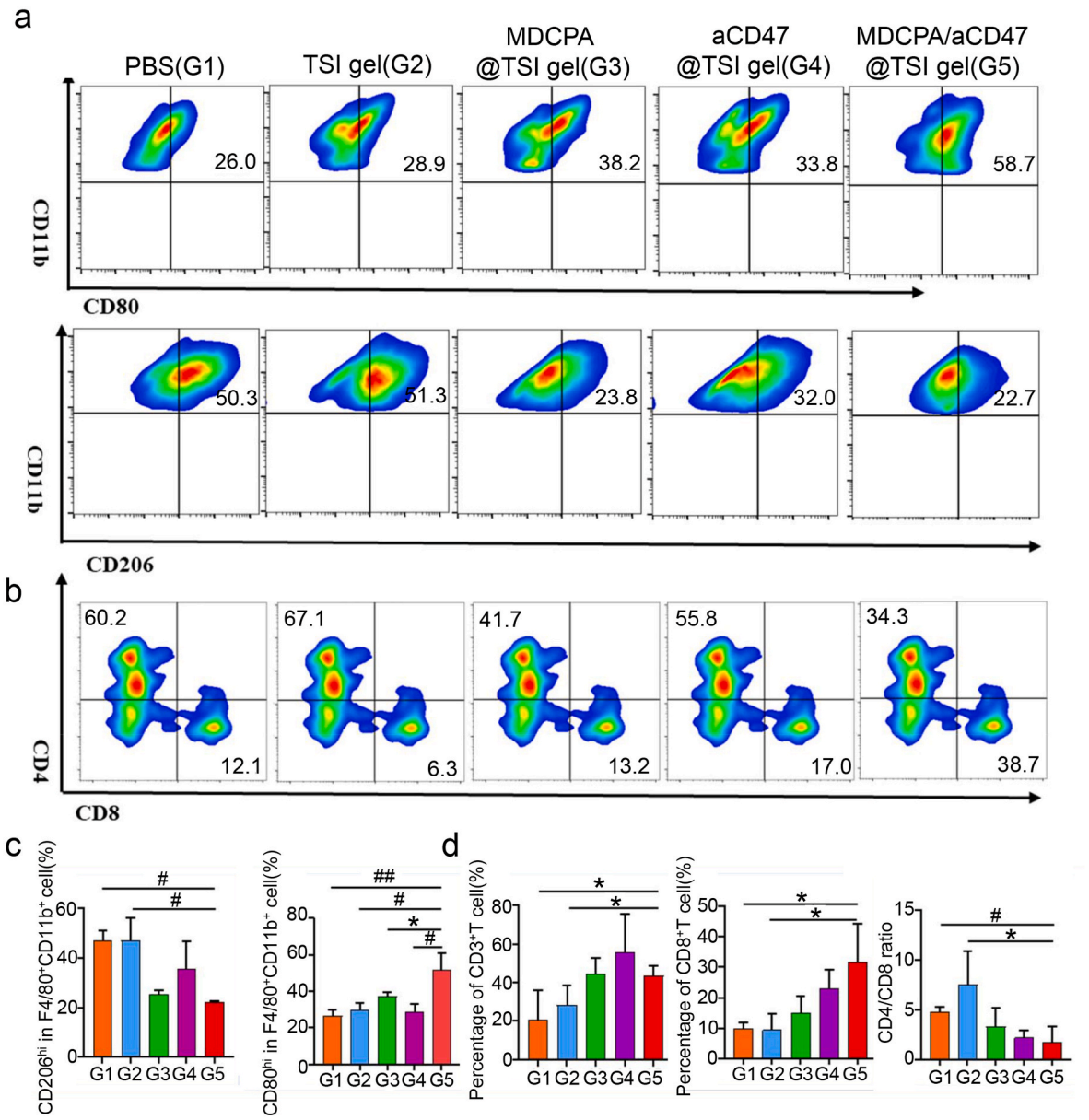

Fig. 6. Representative images of tumor tissue. (a) HE (b) TUNEL and (c) Immunofluorescence staining images of tumor tissue (Panck: red, F4/80: orange, CD86: green, CD163: yellow).

group(G1) (Fig. S9), indicating no material-induced systemic toxicity. These results demonstrated that MDCPA/aCD47@TSI gel can suppress the progression of bone-metastatic prostate cancer with no significant toxicity.

2.7. MDCPA/aCD47@TSI gel induced anti-tumor immune response

To further evaluate the inhibitory effect of the gel on tumors, histological staining of tumor tissue was conducted. The HE staining results shown in Fig. 6a revealed that a greater number of cells exhibited strongly eosinophilic cytoplasm (pink) and shrunken nuclei in the MDCPA/aCD47@TSI gel group compared to the other groups, indicating significant cell apoptosis. TUNEL staining in Fig. 6b further demonstrated a substantial presence of TUNEL-positive cells in the MDCPA/aCD47@TSI gel group, while only a limited number were observed in the other groups. These results suggest that the MDCPA/aCD47@TSI gel significantly inhibited tumor cell proliferation. Additionally, MDCPA has been shown to enhance anti-tumor immunity by inducing macrophage polarization *in vitro* (Fig. 3). The polarization of M1/M2 macrophages [53] was assessed through immunofluorescence staining of CD86 (M1 macrophage marker) and CD206 (M2 macrophage marker) *in vivo*(Fig. 6c). Compared to the PBS group, the number of CD86-positive cell (green) significantly increased, while CD206-positive cell (yellow) significantly decreased in the gel groups. Notably, in the MDCPA/aCD47@TSI gel group, the number of CD86-positive cells was significantly greater than that of CD206-positive cells in the merged image, indicating that the MDCPA/aCD47@TSI gel significantly induced M1 macrophage polarization *in vivo*, which elucidates its potent anti-cancer effects. This finding was further confirmed by the flow cytometric analysis of intratumoral macrophages presented in Fig. 7a–c, which illustrated that the percentage of CD80-positive macrophages was higher and CD206-positive macrophages lower in the MDCPA/aCD47@TSI gel(G5) group compared to the other groups, suggesting that MDCPA/aCD47@TSI gel promotes macrophage polarization towards the M1 phenotype.

In addition to M1 macrophages, T cells can also exert indirect anti-

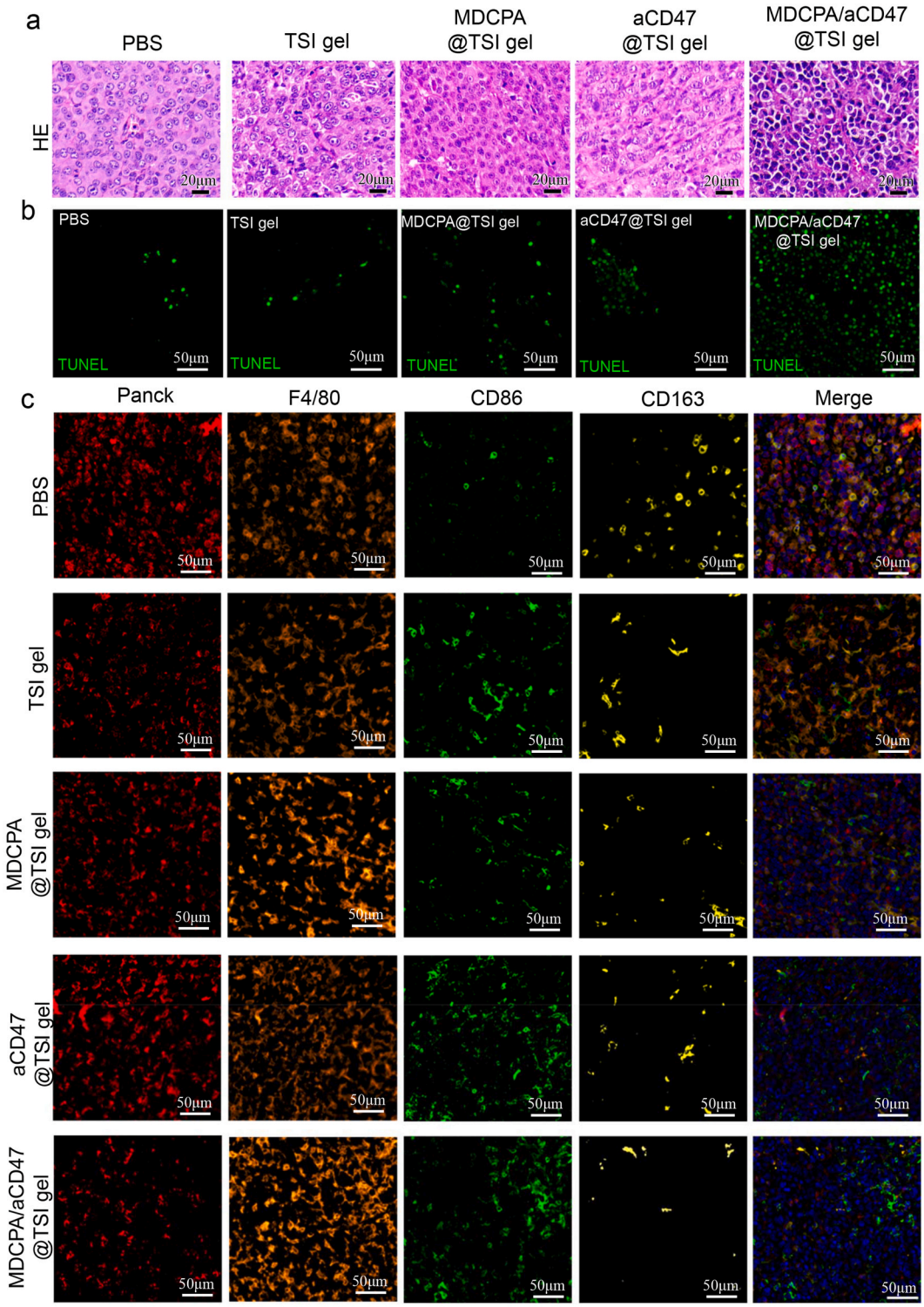

Fig. 7. Anti-tumor immune response induced by MDCPA/aCD47@TSI gel. (a, c) Representative flow cytometric analysis images and elative quantification of M1-like macrophages (CD80hi) gated on F4/80^{+}CD11b^{+}cells. Data are presented as mean ± s.e.m. (n = 4). (b, d) Representative flow cytometric analysis images and relative quantification of CD4^{+}T cells and CD8^{+}T cells gated on CD3^{+}cells. Data are presented as mean ± s.e.m. (n = 3).

tumor effects [54]. A reanalysis of previous single-cell datasets (GSE143791) indicates that the number of CD8+T cells in tumor groups is significantly lower than that in benign groups (Fig. S9), suggesting that the activated CD8^{+} T cells can inhibit the progression of tumor cells. To assess the changes in the number of intratumoral T cells within the tumor, cells obtained from tumors were analyzed using flow cytometry (Fig. 7b–d). The results demonstrated that the percentage of CD3-positive T cells and CD8-positive killer T cells was significantly higher in the MDCPA@TSI gel(G3), aCD47@ TSI gel(G4) and MDCPA/aCD47@TSI gel(G5) groups compared to the PBS(G1) and TSI gel(G2) groups. Furthermore, among the G3, G4 and G5 groups, the percentage of CD8-positive killer T cells increased in the following order: G5>G4>G3, indicating that the G5 group significantly enhanced the proliferation activity of T cells and killer T cells, thereby enhanced

the anti-cancer effect in cooperation with M1 macrophages [55].

2.8. MDCPA/aCD47@TSI gel inhibited bone loss

To confirm the inhibitory effect of MDCPA/aCD47@TSI gel on prostate cancer, proximal tibial bone resorption was evaluated. Firstly, digital photographs of tibias following treatment with different gels are presented in Fig. 8a, while illustrates a decrease in both the length and diameter of the tibia in across all groups. The 3D reconstruction of the proximal tibia in Fig. 8b highlights the bone destruction caused by tumors. Additionally, the longitudinal section of the proximal tibia further reveals cortical bone resorption (indicated by the white arrow). In the MDCPA/aCD47@TSI gel group, although some cortical bone resorption was observed, the cortical bone layer remained largely intact, suggesting

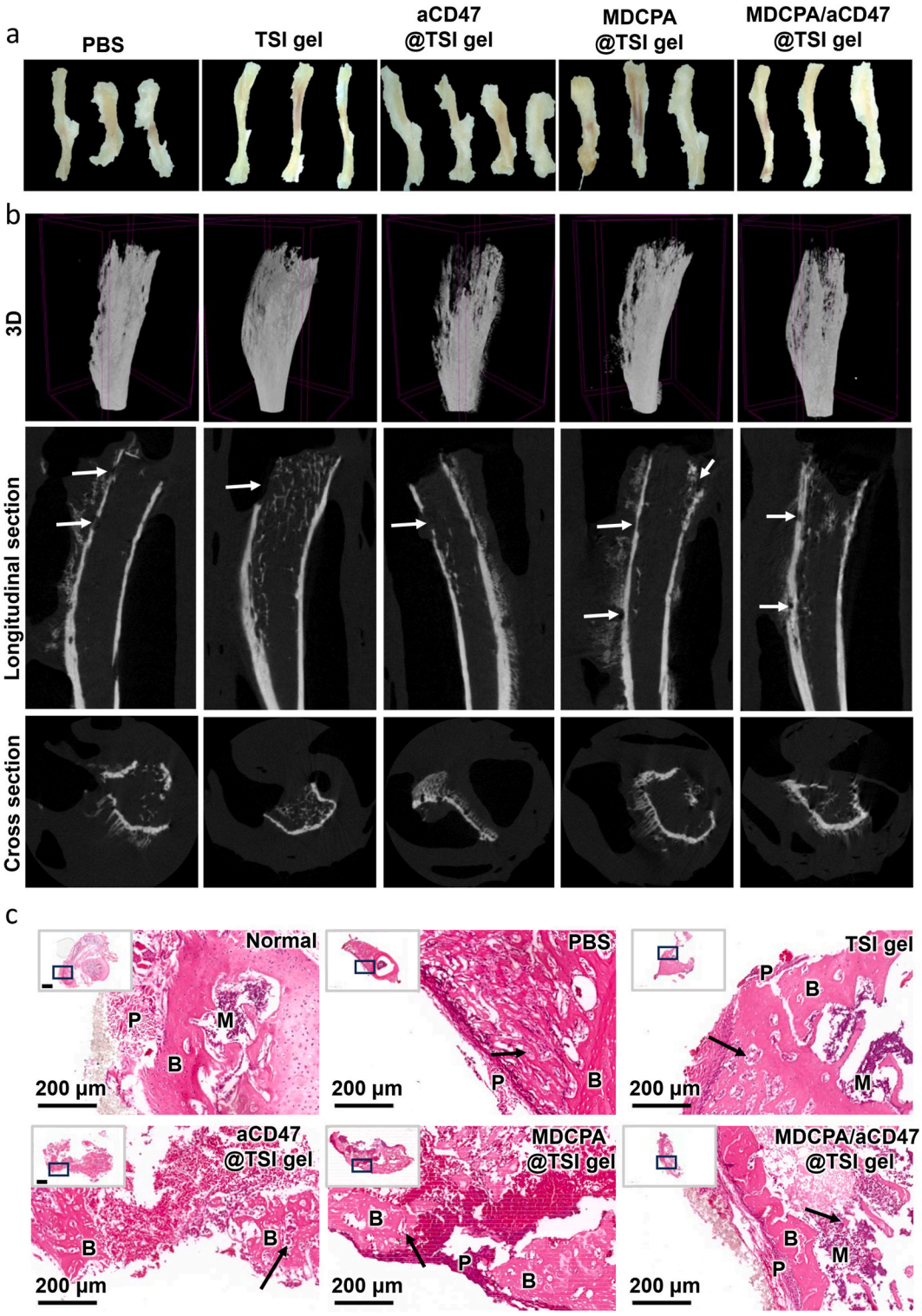

Fig. 8. The effect of different gel treatment on the tibia of mice with bone metastases from prostate cancer. (a) Digital photos of tibia, (b) images-based 3D reconstruction of representative tibia, (c) HE staining of tibia. Visible in the figure is eroded bone (arrow). P: Periosteum, M: marrow, B: bone.

that the combination of MDCPA and aCD47 can effectively inhibited tumor progression and slowed bone resorption. In contrast, the cortical bone in the other groups was incomplete. This finding aligns with the cross-sectional results from the 3D reconstruction, which also demonstrated that only the MDCPA/aCD47@TSI gel group exhibited a relatively complete cortical bone cross-section. To further validate whether the combination of MDCPA and aCD47 can reduce bone resorption, HE staining was performed and is depicted in Fig. 8c. The staining revealed that the structure of the proximal tibia can be divided into three sequential parts from the outside to the inside: Periosteum(P), Bone(B) and Marrow(M). All groups showed bone resorption as indicated by the black arrow, while only MDCPA/aCD47@TSI gel group remained the relatively complete structure including P, B and M. indicating that bone resorption was indeed slowed in this group. Collectively, these results demonstrated that neither MDCPA nor aCD47 alone can effectively inhibit bone resorption; their efficacy is only realized when used in combination.

3. Conclusion

In this study, we report a biomimetic organic-inorganic complex (MDCPA) that utilizes Zein as a biomacromolecule template to effectively stimulate M1 polarization in macrophages, thereby exerting anti-tumor immune effects. *In vitro* experiments demonstrated that MDCPA can induce M1 macrophage polarization and IL-6 secretion while being engulfed, enhancing the phagocytic activity of M1 macrophages against prostate cancer cells. More importantly, when combined with an immune checkpoint inhibitor (aCD47), macrophages exhibited the strongest phagocytic effect on prostate cancer cells. Further *in vivo* experiments revealed significant tumor suppression and reduced bone resorption in a prostate cancer bone metastases model using MDCPA/aCD47 containing thermos-sensitive injectable hydrogels (MDCPA/aCD47 TSI gel). Mechanistic studies indicated that the MDCPA/aCD47 TSI gel induces apoptosis in tumor cells not only through the phagocytosis of M1 macrophages; but also by activating CD8-positive T cells. Our work provides a theragnostic strategy for bone-metastatic prostate cancer by employing biomimetic minerals to mediated anti-tumor immunity, thus overcoming the limitations of conventional M1 macrophage activators, which have inevitable side effects. Moreover, further exploration of long-term effects and systemic responses of MDCPA/aCD47 TSI gel is necessary to assess clinical viability.

4. Experimental section

4.1. Materials and cell line

Zein was purchased from Sinopharm Chemical Reagent Company. Hyaluronic acid (Mw: 800–1000 kDa) was obtained from Shanghai Macklin Biochemical Co., Ltd (Macklin). Pluronic F-127 was acquired from Sigma Chemical Company (Sigma-Aldrich). IL-6 and IL-10 ELASA Kit were all purchased from Beijing Solarbio Science & Technology Co., Ltd, China. aCD47, FITC anti-mouse CD3, PE anti-mouse/human CD11b, APC anti-mouse F4/80, APC anti-mouse CD8a, PE/Cyanine7 anti-mouse CD80, PE/Cyanine7 anti-mouse CD4, PE/Cyanine7 anti-mouse CD206 (MMR)was purchased from Biolegend. (cat. no. 127517, Clone, miap301, cat. no.100203, Clone, 17A2, cat. no.101208, Clone, M1/70, cat. no.13110, Clone, BM8, cat. no. 100711, Clone,53–6.7 cat. no. 104734, Clone, 16-10A1, cat. no. 116016, Clone, RM4-4, cat. no. 1141720, Clone, C068C2) RM-1 mouse prostate cancer cells (RM-1), purchased from Pricella Life Science&Technology Co.,Ltd, is an epithelial-like adherent cell from murine prostate cancer. Cells were cultured in Dulbecco's modified Eagle medium (Gibco) containing 10 % fetal bovine serum (Excell Bio) and 100 U/ml penicillin (Gibco) in an incubator at 37 °C in 5 % CO_2.

Bone marrow derived macrophages (BMDMs) were obtained from bilateral tibia and tibia of BALB/c mice according to standard protocols [21]. Primary mouse BMDM were cultured in DMEM medium supplemented with 20 ng/ml M-CSF, 10 % fetal bovine serum and 1 % antibiotics for 7 days for follow-up experiments.

4.2. Preparation and characterization of MDCPA

0.1 g of Zein was dissolved in 5 mL of 65 wt% ethanol solution. Then the Zein/ethanol solution was dropped into 300 mL artificial saliva (pH = 6.5, prepared as ISO 10271 standards [56]). After standing for 1 h, the artificial saliva was heated to 37 °C with magnetic stirring for 50 rpm. Subsequently, after mineralization for 3 days, the artificial saliva was removed and the MDCPA was obtained by washing the sediment at the bottom using 65 wt% ethanol solution and absolute alcohol.

The phase composite of MDCPA was conducted in X-ray diffraction analysis (XRD, PANalytical, Holland) with measurement angle range from 10 to 70°. Thermogravimetric analysis (TGA) of MDCPA was conducted in thermogravimetric analyzer(Pyris1, USA) under air atmosphere at the heating rate of 10 °C/min from room temperature to 500 °C. The surface morphology and surface element distribution of MDCPA were determined by using Field emission scanning electron microscope (FSEM, Nova NanoSEM 450, Holland) equipped with EDS.

4.3. Biomineralization process of MDCPA

MDCPA, which was synthesized after dripping the ethanol solution containing Zein into the artificial saliva for 5 min and 60 min, respectively, was were collected using a small piece of silicon chip and observed using SEM. MDCPA collected after mineralization for 60 min was dispersed in absolute ethanol and placed on a copper mesh grid for TEM (Talos F200X, Holland) observation. Dark field mode and elemental mapping were conducted for the analysis of calcium and phosphorus deposited on Zein. MDCPA after mineralization for 3 days was collected and stained with calcein solution (1 mg/ml) and tritc phalloidin (100 nM), respectively. After washing with deionized water, MDCPA was analyzed by confocal laser scanning microscope (CLSM, Leica, STELLARIS 5).

4.4. The evaluating of bioactivity

The Ca^{2+} and PO_4^{3-} ions release behaviour of mineral was conducted in SBF (pH = 7.4), which was prepared as the literature reported [57]. 0.01g MDCPA or DCPA was soaked in 5 mL SBF and placed in an incubator at 37 °C water bath. The solution was collected at different predetermined timepoints and replaced with fresh 5 mL SBF. Subsequently, the concentrations of Ca^{2+} and PO_4^{3-} in the collected solutions were measured using calcium assay kit (Beyotime, China) and phosphate assay kit(BioAssay Systems, USA), respectively.

The biomineralization activity of mineral was conducted in SBF. 0.01g MDCPA or DCPA was soaked in SBF(5 mL) and placed in an incubator at 37 °C water bath for 7 days. The solution was replaced with fresh 5 mL SBF every two days. Then the mineralized samples were collected and dried in an oven at 60 °C for XRD, FTIR(Nicolet iS50R, USA), SEM and TEM analysis.

4.5. Preparation of calcein-labeled mineral suspensions

0.2 g MDCPA or DCPA particles were mixed with 1 mL of 0.1 mg/mL calcein solution and incubated in a shaker for 30 min at room temperature, protected from light. After centrifugation at 8000 rpm for 5min, the supernatant was discarded, and calcein-labeled mineral particles were obtained by washing with deionized (DI) water and dried at 60 °C overnight. Subsequently, 0.01g calcein-labeled mineral particles were sterilized using autoclave sterilization and dispersed in 10 mL DMEM to obtain a suspension at a concentration of 1000 μg/mL.

4.6. Macrophages mediated mineral particle phagocytosis in vitro

RAW264.7 cells were seeded in confocal dishes at a density of 2 × 10^4 cells per well. After 24 h of incubation, the calcein-labeled MDCPA or DCPA suspensions were added. Then the colocalization between calcein-labeled MDCPA particles and cells was examined using confocal microscope at 0, 5, 15, 30 and 35 min. The initial contact time between the particle and the cell was recorded as 0 min.

For fluorescent microscope analysis, RAW264.7 cells were seeded in a 24-well plate at a density of 1 × 10^5 cells per well. Subsequently, calcein-labeled mineral suspensions with a concentration of 125 μg/mL were added. After cultured for 6 h, cells were fixed using 4 % para-formaldehyde solution and then stained using DAPI (AC0065, Acmec, China) and rhodamine phalloidin. The colocalization between MDCPA particles and cells was observed under fluorescence microscope (Leica DMi8, GER).

4.7. Gene expression in macrophages following stimulation of mineral particle

RAW264.7 cells were seeded in a 6-well plate at a density of 5 × 10^5 cells per well. After incubation overnight, mineral suspensions with a concentration of 125 μg/mL were added. After cultured for 24 h, total RNAs were extracted for the determination of expression of IL-6, IL-10, CD206 and CCR7 genes via qRT-PCR (Roche LoghtCycler 96, CH). The 2-ΔΔCt method was applied to compare the mRNA expression levels. The details of primers were shown in Table S1.

4.8. ELASA analysis

RAW264.7 cells were seeded in a 6-well plate at a density of 1 × 10^5 cells. Then the complete media was replaced by complete media with LPS (1000 μg/mL)、IL-4 (20 nM) or MDCPA suspensions (125 μg/mL). After 6 h, the cell supernatant was collected and filtrated through a bacterial filter. The concentration of IL-6 and IL-10 in cell supernatant were detected by ELASA assay (SAB, USA).

4.9. RNA sequencing of macrophages

RAW264.7 cells were plated in a 6-well plate at a density of 1 × 105 cells per well and cultured overnight. Subsequently, the culture medium was replaced with complete media or MDCPA suspension 125 μg/mL. After a 1-day incubation period, total RNA was extracted. RNA integrity was evaluated using the RNA Nano 6000 Assay Kit on a Bioanalyzer 2100 system (Agilent Technologies). FeatureCounts v1.5.0-p3 was utilized to quantify the number of reads mapped to each gene. The fragments per kilobase of transcript per million mapped reads (FPKM) for each gene were calculated based on the gene's length and the mapped read count. Differential expression analysis between the groups, each containing three biological replicates, was conducted using the DESeq2 R package (version 1.20.0). Significant DEGs were identified with a threshold of $|log2FC| > 1$ and $p < 0.05$. GO and KEGG enrichment analysis of the DEGs was performed using the clusterProfiler R package, correcting for gene length bias. GO and KEGG terms with corrected p-values <0.05 were deemed significantly enriched by the DEGs.

4.10. Phagocytosis in vitro

BMDM was co-cultured with MDCPA for 24h, and then stained with PKH67 and RM-1 cells were stained with DiL. RM-1 cells(4 × 10^5) pre-blocked with IgG or aCD47 were co-cultured with macrophages(1 × 10^5) in serum-free medium for 2h at 37 °C. Phagocytosis efficiency was observed by the fluorescence microscope or CytoFLEX flow cytometry (Beckman, US).

4.11. Preparation of thermo-sensitive injectable hydrogel (TSI gel)

The Gel was prepared as the literature [52] but some modification. The Gel was prepared simply by mixing Hyaluronic acid (0.0113g), Pluronic F-127 (0.17 g) and DMEM (1 mL) to obtain a clear solution.

4.12. Measurement of clouding temperature (CT) of TSI gel

The turbidimetry method was employed to measure the CT values of TSI gel. The optical transmittance change of TSI gel was measured at 500 nm wavelength by using an UV–vis spectrophotometer (UV-2450, Shimadzu, Japan) at increasing temperatures (24–40 °C, Equilibrium time: 2 °C/10 min).

4.13. aCD47 loaded in gel

The aCD47 loaded hydrogel (aCD47@TSI gel) with or without MDCPA were prepared using the Gel. Briefly, 50 μL aCD47 solution was mixed with 450 μL Gel to obtain aCD47@TSI Gel. MDCPA contained aCD47/Gel (MDCPA/aCD47@TSI gel) was prepared by mixing 6 mg MDCPA with above 500 μL aCD47@TSI gel.

4.14. In vitro drug release study

The aCD47 release testing of aCD47/TSI gel and MDCPA/aCD47/TSI gel was carried out by using a dialysis tube (molecular weight cut off, MWCO: 100 KDa). In detail, 100 μL gels was added to dialysis tube and then incubated in 60 mL of SBF (pH 7.2, prepared as the literature [58]) at 37 °C with continuous agitation (50 rpm). At each time (1h, 3h, 6h, 12h, 24h, 72h, 120h and 168h), 500 μL SBF was collected and 500 μL of fresh SBF was added. Finally, the amount of released aCD47 was determined using aCD47 ELASA Kit (Solarbio, China).

4.15. Construction of bone-metastatic prostate cancer model

Male Balb/c mice (6–10 weeks) were purchased from Guangdong Medical Laboratory Animal Center. This experiment has been approved by the Ethics Committee of Guangdong Provincial People's Hospital (KY-Q-2022-425). For the constructing of prostate cancer bone metastasis model, 50 μL RM-1-Luc cell suspension (1 × 10^6 cells/mL) was inoculated into the right tibia of male C57 mice. Bioluminescence imaging was used to observe the tumor growth rate at 7, 10, 13 days after inoculation. Before the bioluminescence imaging, each mouse was intraperitoneally injected with 10 μL/g DPBS dissolved with a concentration of 15mg/ml D-luciferin potassium salt. The tumor size was observed using the In Vivo Iimaging System (IVIS Spectrum, PerkinElmer).

4.16. In vivo antitumor efficacy

Five experiment groups were designed: PBS group, TSI gel group, MDCPA@TSI gel group, CD47@TSI gel group and MDCPA/aCD47@TSI gel group. All operations were carried out on the clean bench. In detail, PBS and TSI gel were all sterile processed through a 0.22 μm bacterial filter. For MDCPA@TSI gel group, 3 mg MDCPA particles were added to 1 mL TSI gel and mixed well. For CD47@TSI gel group, 200 μL 50 μg/40 μL aCD47 were added to 800 μL TSI gel and mixed well. For MDCPA/aCD47@TSI gel, 3 mg MDCPA particles and 200 μL 50 μg/40 μL aCD47 were both added to 800 μL TSI gel and mixed well. Then 1 mL sterile syringe loaded 1 mL volume of solution or gel above were prepared and placed at 4 °C before use. To evaluate the antitumor effect, four C57 mice with bone-metastatic prostate cancer pre group were used. 200 μL PBS or other gels were applied in one mouse via intratumoral injection. After day 0, day 3 and day 6, the therapeutic effect was assessed by bioluminescence imaging and the statistical analysis of total flux.

4.17. Flow cytometry

Tumors collected from mice were divided into small pieces and digested with digestive enzymes to make single-cell suspension. Flow cytometry antibodies with different fluorescent labels were diluted according to the dilution ratio recommended by the reagent manufacturer to stain the cells: FITC anti-mouse CD3, PE anti-mouse/human CD11b, APC anti-mouse F4/80, APC anti-mouse CD8a, PE/Cyanine7 anti-mouse CD80, PE/Cyanine7 anti-mouse CD4, PE/Cyanine7 anti-mouse CD206 (MMR). The stained cells were measured on CytoFLEX flow cytometry (Beckman, US) and analyzed by FlowJo software (version 10.0.7, TreeStar). Flow cytometry analyses the numbers shown in the images on a percentage-based basis.

4.18. Immunofluorescence staining

Tumor samples of mice in each group were collected, and the abundance of different immune cell infiltration was detected by multiple immunofluorescences. The tumor tissue was fixed with 4 % paraformaldehyde and then paraffin embedded and sliced. The prepared tumor sections were stained according to the instructions of the Multiple fluorescent immunohistochemical staining Kit (Absin), sealed with TBST containing 5 % goat serum, and then incubated with antibodies. The antibodies included PanCK (Absin, abs123684, 1:400), F4/80 (CST,70076, 1:300), CD86(CST, 19589, 1:200), and CD163(Abcam, ab182422,1:500). The nuclei were stained with DAPI before sealing and all sections were scanned with a fluorescence scanning camera (KFBIO, KF-TB-400).

4.19. Assessment of in vivo biocompatibility

After intratumoral injection with different gels for 7 days as 5.16, the whole blood of four mouse per groups were collected before execution, and the samples were left at room temperature for 2 h and centrifuged at 3000 rpm at 4 °C for 15 min. The supernatants were used to determine the levels of alanine aminotransferase (ALT) and aspartate aminotransferase (AST) using Fully Automatic biochemistry analyzer (Rayto, Chemray 240).

4.20. Micro-CT and histological analysis

After the tumor was removed at day 6, the tibia was collected and fixed using polyformaldehyde solution (4 % in PBS) for 24 h. Then the tibia was analyzed by Micro-CT (SKYSCAN 1276, Bruker). For histological analysis, the tibia was embedded in paraffin after decalcification and gradient ethanol dehydration. Sections were cut in distal tibia and stained with H&E staining kit. A digital pathology slide Scanner (Aperio Versa, Leica) was used to observe and image the sections.

4.21. Statistical analysis

All results are presented as the mean ± standard error of the mean (s.e.m.), as indicated. Tukey post-hoc tests and one-way ANOVA were used for multiple comparisons (when more than two groups were compared), and Student's test was used for two-group comparisons. All statistical analyses were carried out with Prism software package (PRISM 9.0; GraphPad Software, 2020). The threshold for statistical significance was $^{*}p < 0.05$, $^{\#}p < 0.01$, $^{\#\#}p < 0.001$.

CRediT authorship contribution statement

Shenglong Tan: Writing – original draft, Supervision, Methodology, Funding acquisition, Data curation, Conceptualization. **Qianqian Wang:** Validation, Supervision, Methodology, Data curation, Conceptualization. **Chunxiang Feng:** Supervision, Methodology, Funding acquisition, Data curation, Conceptualization. **Xiaoyong Pu:** Supervision, Methodology. **Dong Li:** Supervision, Methodology, Funding acquisition. **Fenglian Jiang:** Supervision, Methodology, Funding acquisition. **Jian Wu:** Supervision, Methodology, Funding acquisition. **Shang Huang:** Supervision, Methodology, Funding acquisition. **Junhong Fan:** Data curation, Methodology. **Ruijuan Zhong:** Data curation, Methodology. **Chunmiao Mo:** Supervision, Methodology. **Jiayu Luo:** Supervision, Methodology. **Peiliang Zhong:** Supervision, Methodology. **Jiumin Liu:** Writing – review & editing, Supervision, Methodology, Funding acquisition. **Dandan Ma:** Writing – review & editing, Supervision, Methodology, Funding acquisition.

Permission to reproduce material from other sources

The data that supports the findings of this study are available in the supplementary material of this article.

Declaration of competing interest

There are no conflicts to declare.

Acknowledgements

This research was funded by the National Natural Science Foundation of China (Grant Nos. 82201133), Guangzhou Basic and Applied Basic Research Foundation(2024A04J6614), The Project of Guangdong Provincial Department of Finance (No. KS0120220267; No. KS0120220269; No. KS0120220270; No. KS0120220271; No. KS0120220272), Guangzhou Basic and Applied Basic Research Foundation (No. 202201011030), Science and Technology Program of Guangzhou (No. 2023NS227010).

Appendix A. Supplementary data

Supplementary data to this article can be found online at https://doi.org/10.1016/j.mtbio.2025.101573.

Data availability

Data will be made available on request.

References

[1] A. Berruti, L. Dogliotti, R. Bitossi, G. Fasolis, G. Gorzegno, M. Bellina, M. Torta, F. Porpiglia, D. Fontana, A. Angeli, Incidence of skeletal complications in patients with bone metastatic prostate cancer and hormone refractory disease: predictive role of bone resorption and formation markers evaluated at baseline, J. Urol. 164 (2000) 1248–1253.
[2] R.E. Coleman, P.I. Croucher, A.R. Padhani, P. Clézardin, E. Chow, M. Fallon, T. Guise, S. Colangeli, R. Capanna, L. Costa, Bone metastases, Nat. Rev. Dis. Primers 6 (2020) 83.
[3] M. Bienz, F. Saad, Androgen-deprivation therapy and bone loss in prostate cancer patients: a clinical review, BoneKEy Rep. 4 (2015) 716.
[4] Y. Mano, S. Aishima, N. Fujita, Y. Tanaka, Y. Kubo, T. Motomura, A. Taketomi, K. Shirabe, Y. Maehara, Y. Oda, Tumor-associated macrophage promotes tumor progression via STAT3 signaling in hepatocellular carcinoma, Pathobiology 80 (2013) 146–154.
[5] R. Hughes, B.Z. Qian, C. Rowan, M. Muthana, I. Keklikoglou, O.C. Olson, S. Tazzyman, S. Danson, C. Addison, M. Clemons, A.M. Gonzalez-Angulo, J. A. Joyce, M. De Palma, J.W. Pollard, C.E. Lewis, Perivascular M2 macrophages stimulate tumor relapse after chemotherapy, Cancer Res. 75 (2015) 3479–3491.
[6] Z. Duan, Y. Luo, Targeting macrophages in cancer immunotherapy, Signal Transduction Targeted Ther. 6 (2021) 127.
[7] Y. Wang, C. Zhao, Y. Liu, C. Wang, H. Jiang, Y. Hu, J. Wu, Recent advances of tumor therapy based on the CD47-SIRPα Axis, Mol. Pharm. 19 (2022) 1273–1293.
[8] L. Zhai, Y. Shi, Y. Yan, A. Lu, X. Liu, L. Lei, Y. Sun, L. Jiang, X. Wang, H. Qian, J. Wang, Local sustained release of PD-1 monoclonal antibody and lenvatinib by thermo-sensitive hydrogel for improving tumor immunotherapy, Chin. Chem. Lett. 34 (2023) 108104.
[9] J. Huang, B. Yue, J. Sun, T. Xu, J. Zhou, L. Lu, Y. Yan, J.F. Lovell, C. Wan, M. Zhu, H. Jin, Injectable thermosensitive hydrogels loaded with irradiated tumor cell-derived microparticles and manganese activate anti-tumor immunity, Nano Today 58 (2024) 102455.

[10] S. Tanga, M. Aucamp, P. Ramburrun, Injectable thermoresponsive hydrogels for cancer therapy: challenges and prospects, Gels 9 (2023).
[11] J.Y. Lee, K.S. Kim, Y.M. Kang, E.S. Kim, S.-J. Hwang, H.B. Lee, B.H. Min, J.H. Kim, M.S. Kim, In vivo efficacy of paclitaxel-loaded injectable in situ-forming gel against subcutaneous tumor growth, Int. J. Pharm. 392 (2010) 51–56.
[12] D. Aminin, Y.-M. Wang, Macrophages as a "weapon" in anticancer cellular immunotherapy, The Kaohsiung J Res Med Sci 37 (2021) 749–758.
[13] A. Kresinsky, N. Schneble, C. Schmidt, A. Frister, R. Bauer, R. Wetzker, J.P. Müller, Phagocytosis of bone marrow derived macrophages is controlled by phosphoinositide 3-kinase γ, Immunol. Lett. 180 (2016) 9–16.
[14] R.J. Soiffer, K.A. Kooshesh, V. Ho, Whole tumor cell vaccines engineered to secrete GM-CSF (GVAX), ImmunoMedicine 1 (2021) e1025.
[15] P. Lapidari, I. Vaz-Luis, A. Di Meglio, Side effects of using granulocyte-colony stimulating factors as prophylaxis of febrile neutropenia in cancer patients: a systematic review, Crit. Rev. Oncol. Hematol. 157 (2021) 103193.
[16] A. Hanlon, D.M. Brander, Managing toxicities of phosphatidylinositol-3-kinase (PI3K) inhibitors, Hematology 2020 (2020) 346–356.
[17] L. Xiao, Y. Shiwaku, R. Hamai, K. Tsuchiya, K. Sasaki, O. Suzuki, Macrophage polarization related to crystal phases of calcium phosphate biomaterials, Int. J. Mol. Sci. 22 (2021) 11252.
[18] L. Xiao, Y. Shiwaku, R. Hamai, K. Baba, K. Tsuchiya, S. Imazato, K. Sasaki, O. Suzuki, Osteogenic capacity of octacalcium phosphate involving macrophage polarization, J. Biomed. Mater. Res. 111 (2023) 1006–1020.
[19] K. Chen, Q. Man, J. Miao, W. Xu, Y. Zheng, X. Zhou, Z. Gao, Kir2.1 channel regulates macrophage polarization via the Ca2+/CaMK II/ERK/NF-κB signaling pathway, J. Cell Sci. 135 (2022) jcs259544.
[20] J. Mo, Y. Xu, X. Wang, W. Wei, J. Zhao, Exploiting the protein corona: coating of black phosphorus nanosheets enables macrophage polarization via calcium influx, Nanoscale 12 (2020) 1742–1748.
[21] A. Grandjean-Laquerriere, O. Tabary, J. Jacquot, D. Richard, P. Frayssinet, M. Guenounou, D. Laurent-Maquin, P. Laquerriere, S. Gangloff, Involvement of toll-like receptor 4 in the inflammatory reaction induced by hydroxyapatite particles, Biomaterials 28 (2007) 400–404.
[22] Y. Hua, J. Wu, H. Wu, C. Su, X. Li, Q. Ao, Q. Zeng, X. Zhu, X. Zhang, Exposure to hydroxyapatite nanoparticles enhances Toll-like receptor 4 signal transduction and overcomes endotoxin tolerance in vitro and in vivo, Acta Biomater. 135 (2021) 650–662.
[23] F. Tamimi, J. Torres, D. Bassett, J. Barralet, E.L. Cabarcos, Resorption of monetite granules in alveolar bone defects in human patients, Biomaterials 31 (2010) 2762–2769.
[24] B. Idowu, G. Cama, S. Deb, L. Di Silvio, In vitro osteoinductive potential of porous monetite for bone tissue engineering, J. Tissue Eng. 5 (2014) 2041731414536572.
[25] H. Zhou, L. Yang, U. Gbureck, S.B. Bhaduri, P. Sikder, Monetite, an important calcium phosphate compound–Its synthesis, properties and applications in orthopedics, Acta Biomater. 127 (2021) 41–55.
[26] B. Kruppke, J. Farack, A.S. Wagner, S. Beckmann, C. Heinemann, K. Glenske, S. Rossler, H.P. Wiesmann, S. Wenisch, T. Hanke, Gelatine modified monetite as a bone substitute material: an in vitro assessment of bone biocompatibility, Acta Biomater. 32 (2016) 275–285.
[27] Z. Sheikh, M.-N. Abdallah, A. Hanafi, S. Misbahuddin, H. Baloch, M. Glogauer, Mechanisms of in vivo degradation and resorption of calcium phosphate based biomaterials, Materials 8 (2015) 7913–7925.
[28] S. Wenisch, J.P. Stahl, U. Horas, C. Heiss, O. Kilian, K. Trinkaus, A. Hild, R. Schnettler, In vivo mechanisms of hydroxyapatite ceramic degradation by osteoclasts: fine structural microscopy, J. Biomed. Mater. Res. 67 (2003) 713–718.
[29] H. Zhou, L. Yang, U. Gbureck, S.B. Bhaduri, P. Sikder, Monetite, an important calcium phosphate compound-Its synthesis, properties and applications in orthopedics, Acta Biomater. 127 (2021) 41–55.
[30] S.Y. Li, Y.L. Guo, J.W. Tian, H.J. Zhang, R.F. Li, P. Gong, Z.L. Yu, Anti-tumor strategies by harnessing the phagocytosis of macrophages, Cancers 15 (2023).
[31] R. Mulongo-Masamba, T. El Kassri, M. Khachani, S. Arsalane, M. Halim, A. El Hamidi, Synthesis and thermal dehydroxylation kinetic of anhydrous calcium phosphate monetite CaHPO4, J. Therm. Anal. Calorim. 124 (2016) 171–180.
[32] K. Suchanek, A. Bartkowiak, M. Perzanowski, M. Marszalek, From monetite plate to hydroxyapatite nanofibers by monoethanolamine assisted hydrothermal approach OPEN, Sci. Rep. 8 (2018) 15408.
[33] D.E. Fleming, W. van Bronswijk, R.L. Ryall, A comparative study of the adsorption of amino acids on to calcium minerals found in renal calculi, Clin. Sci. (Lond.) 101 (2001) 159–168.
[34] Z. Wang, Z. xu, W. Zhao, N. Sahai, A potential mechanism for amino acid-controlled crystal growth of hydroxyapatite, J. Mater. Chem. B 3 (2015).
[35] Y. Li, C. Yao, Mineralization of hydroxyapatite crystallites on zein microspheres, Polym. Compos. 33 (2012).
[36] C.-Y. Zhang, W. Zhang, L.-b. Mao, Y. Zhao, S.-H. Yu, Biomimetic mineralization of zein/calcium phosphate nanocomposite nanofibrous mats for bone tissue scaffold, CrystEngComm 16 (2014).
[37] T. Song, Z. Xiong, T. Shi, L. Yuan, R. Gao, Effect of glutamic acid on the preparation and characterization of Pickering emulsions stabilized by zein, Food Chem. 366 (2022) 130598.
[38] P. Ustriyana, F. Schulte, F. Gombedza, A. Gil-Bona, S. Paruchuri, F.B. Bidlack, M. Hardt, W.J. Landis, N. Sahai, Spatial survey of non-collagenous proteins in mineralizing and non-mineralizing vertebrate tissues ex vivo, Bone Rep 14 (2021) 100754.
[39] K.V. Nishad, S. Sureshbabu, M. Komath, G. Unnikrishnan, Synthesis and characterization of low dimensional bioactive monetite by solvent exchange method, Mater. Lett. 209 (2017) 19–22.
[40] T. Kokubo, H. Takadama, Simulated Body Fluid (SBF) as a Standard Tool to Test the Bioactivity of Implants, Handbook of Biomineralization, 2007.
[41] M.S.M. Arsad, P.M. Lee, Synthesis and characterization of hydroxyapatite nanoparticles and β-TCP particles, Colloids Surf. 322 (2008) 29–33.
[42] T.A. Masters, B. Pontes, V. Viasnoff, Y. Li, N.C. Gauthier, Plasma membrane tension orchestrates membrane trafficking, cytoskeletal remodeling, and biochemical signaling during phagocytosis, Pros. Natl. Acad. Sci. U.S.A 110 (2013) 11875–11880.
[43] M. Saraiva, A. O'Garra, The regulation of IL-10 production by immune cells, Nat. Rev. Immunol. 10 (2010) 170–181.
[44] M.R. Fernando, J.L. Reyes, J. Iannuzzi, G. Leung, D.M. McKay, The pro-inflammatory cytokine, interleukin-6, enhances the polarization of alternatively activated macrophages, PLoS One 9 (2014) e94188.
[45] M. Wang, F. Chen, Y. Tang, J. Wang, X. Chen, X. Li, X. Zhang, Regulation of macrophage polarization and functional status by modulating hydroxyapatite ceramic micro/nano-topography, Mater. Des. 213 (2022) 110302.
[46] C. Yunna, H. Mengru, W. Lei, C. Weidong, Macrophage M1/M2 polarization, Eur. J. Pharmacol. 877 (2020) 173090.
[47] S. Lin, Z. Zhou, H. Zhao, C. Xu, Y. Guo, S. Gao, X. Mei, H. Tian, TNF promotes M1 polarization through mitochondrial metabolism in injured spinal cord, Free Radic. Biol. Med. 172 (2021) 622–632.
[48] H. Wang, X. Wang, X. Zhang, W. Xu, The promising role of tumor-associated macrophages in the treatment of cancer, Drug Resist, Updat 73 (2024) 101041.
[49] S.M.G. Hayat, V. Bianconi, M. Pirro, M.R. Jaafari, M. Hatamipour, A. Sahebkar, CD47: role in the immune system and application to cancer therapy, Cell. oncol. (Dordr.) 43 (2020) 19–30.
[50] J. Wang, H. Zhang, X. Yin, Y. Bian, Anti-CD47 antibody synergizes with cisplatin against laryngeal cancer by enhancing phagocytic ability of macrophages, Clin. Exp. Immunol. 205 (2021) 333–342.
[51] J. Song, R. Hu, J. Zhang, Y. Yu, Y. Zhou, W. Ding, X. Wang, R. Tang, Thermo-sensitive nanoparticle-hydrogel composite based on pluronic F127 and phycocyanin for an enhanced chemo-photodynamic antitumor effect, ACS Appl. Polym. Mater. 5 (2023) 6244–6254.
[52] Y.-s. Jung, W. Park, H. Park, D.-K. Lee, K. Na, Thermo-sensitive injectable hydrogel based on the physical mixing of hyaluronic acid and Pluronic F-127 for sustained NSAID delivery, Carbohydr. Polym. 156 (2017) 403–408.
[53] Q. Sun, S. Hu, Z. Lou, J. Gao, The macrophage polarization in inflammatory dermatosis and its potential drug candidates, Biomed. Pharmacother. 161 (2023) 114469.
[54] E.M. Garrido-Martin, T.W.P. Mellows, J. Clarke, A.P. Ganesan, O. Wood, A. Cazaly, G. Seumois, S.J. Chee, A. Alzetani, E.V. King, C.C. Hedrick, G. Thomas, P. S. Friedmann, C.H. Ottensmeier, P. Vijayanand, T. Sanchez-Elsner, M1(hot) tumor-associated macrophages boost tissue-resident memory T cells infiltration and survival in human lung cancer, J Immunother Cancer 8 (2020) e000778.
[55] C.G. Cess, S.D. Finley, Multi-scale modeling of macrophage-T cell interactions within the tumor microenvironment, PLoS Comput. Biol. 16 (2020) e1008519.
[56] V. Leung, B. Darvell, Artificial salivas for in vitro studies of dental materials, J. Dent. 25 (1997) 475.
[57] S. Arthanari, R. Nallaiyan, Surface characteristics, corrosion resistance and MG63 osteoblast-like cells attachment behaviour of nano SiO2-ZrO2 coated 316L stainless steel, RSC Adv. 5 (2015) 26007–26016.
[58] A.L.B. Maçon, T. Kim, E. Valliant, K. Goetschius, R. Brow, D. Day, A. Hoppe, A. Boccaccini, I. Kim, C. Ohtsuki, T. Kokubo, A. Osaka, M. Vallet-Regí, D. Arcos, L. Fraile, A. Salinas, A. Teixeira, Y. Vueva, R. Almeida, J. Jones, A unified in vitro evaluation for apatite-forming ability of bioactive glasses and their variants, J. Mater. Sci. Mater. Med. 26 (2015) 5403.